Microfluid Nanofluid (2010) 9:341–355
DOI 10.1007/s10404-009-0551-1

RESEARCH PAPER

Capillary driven movement of gas bubbles in tapered structures

Tobias Metz · Nils Paust · Roland Zengerle · Peter Koltay

Received: 5 September 2009 / Accepted: 30 November 2009 / Published online: 24 December 2009

Abstract This article presents a study on the capillary driven movement of gas bubbles confined in tapered channel configurations. These configurations can be used to transport growing gas bubbles in micro fluidic systems in a passive way, i.e. without external actuation. A typical application is the passive degassing of CO_2 in micro direct methanol fuel cells (μDMFC). Here, a one-dimensional model for the bubble movement in wide tapered channels is derived and calibrated by experimental observations. The movement of gas bubbles is modelled on straight trajectories based on a balance of forces. The bubble geometry is considered as three dimensional. In the development of the model, the effects of surface tension, inertia, viscosity, dynamic contact angle and thin film deposition are considered. It is found that in addition to viscous dissipation, the dynamics related to the contact line—dynamic contact angle and thin film deposition—are essential to describe the gas bubble's movement. Nevertheless, it was also found that both of these effects, as modelled within this work, have similar impact and are hard to distinguish. The model was calibrated against experiments in a parameter range relevant for the application of travelling gas bubbles in passive degassing structures for μDMFCs.

1 Introduction

In the development of micro direct methanol fuel cells (μDMFC), the management of gas bubbles is an important issue. How those gas bubbles appear under different conditions is, e.g. shown by Yang et al. (2004a). Gas bubbles induce strong resistant effects to the flow in the channels and therefore have to be removed. An interesting study on how the resistant effects and the removal of gas bubbles may interact has been shown by Wong et al. (2005a). On the other hand, a certain amount of properly managed gas bubbles can even improve cell performance as shown by Yang et al. (2004b).

In this article, we consider the problem of a gas bubble moving in a tapered channel with wetting walls as shown in Fig. 1. The bubble is initially confined in the narrow end of the tapered channel and moves towards the wider opening of the channel in order to minimize its surface energy.

The described effect was already applied for the passive removal of gas bubbles appearing in the anode flow field of a μDMFC by Litterst et al. (2006) and Paust et al. (2009a, b). In this article, the physical effects that control the gas bubble's movement in such tapered channels are studied, in particular for a channel width that is about ten times the bubble diameter. In such "wide" tapered channels, the influence of the side walls on the bubble movement is negligible. The end position to which a gas bubble moves is given by the position where it exhibits minimum surface energy (Langbein 2002). This equilibrium position can be determined by analytical means as well as by computational fluid dynamics (CFD) using the volume of fluid method and taking into account surface tension and contact angles. The calculation of the dynamics of the equilibration process is, however, much more difficult. Modelling the dynamic movement is, e.g. of relevance for prediction of the time scale of equilibration and thus the gas flow rates which can be achieved by the capillary movement of the gas bubbles. Attempts to model such dynamic processes using the CFD package CFD-ACE+ from ESI-CFD (2006) performed by

T. Metz · N. Paust (✉) · R. Zengerle · P. Koltay
Laboratory for MEMS Applications, Department of Microsystems Engineering (IMTEK), University of Freiburg, Georges-Koehler-Allee 106, 79110 Freiburg, Germany
e-mail: nils.paust@imtek.de

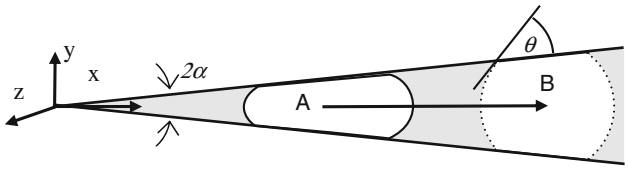

Fig. 1 A squeezed bubble moves from a squeezed position (*A*) to its equilibrium position (*B*)

the authors resulted in too long computational times to be of practical relevance for parameter studies.

In order to model the behaviour of gas bubbles in tapered channel configurations more efficiently, an analytical model is presented in this article. The model considers the dominant effects during travel of a gas bubble. The purpose of the model is to describe the movement of gas bubbles in a relevant parameter space in an efficient way but not to completely explain the underlying physics. The latter would need to use more elaborated models given for the considered effects and derive the necessary physical parameters in a huge series of distinct experiments. Precedence was taken to keep the model simple.

As the movement of gas bubbles is strongly driven by the decrease in surface energy while entering the wider end of the channel, it can be considered mainly as one dimensional. The bubble shape is considered three dimensional and is parameterized as an asymmetric squeezed tin body. The maximum distance a gas bubble of given volume can travel in a tapered channel (Fig. 1) increases when decreasing the tapering angle 2α as the distance of the equilibrium position (B) towards the narrow end increases. In this article, only small tapering angles are considered ($2\alpha < 20°$). Therefore, the configuration is similar to the movement of gas bubbles in Hele-Shaw Cells, sketched in Fig. 2. The movement of gas bubbles in Hele-Shaw Cells has been investigated theoretically by Tanveer (1987), Taylor and Saffman (1959), Saffman and Tanveer (1989) and Tanveer (1986) and by

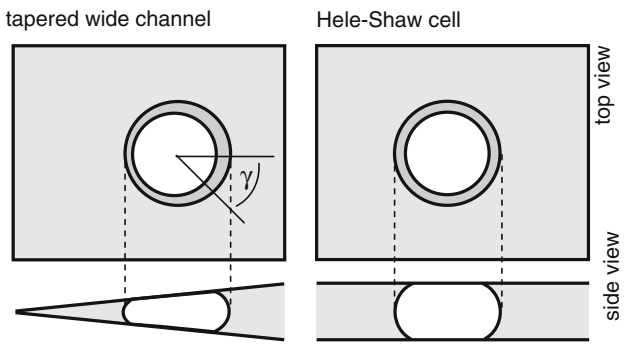

Fig. 2 Sketch of a deformed bubble in a tapered channel and a Hele-Shaw Cell (tin body)

experiments by Kopfsill and Homsy (1988). In a Hele-Shaw Cell, a gas bubble moves between two parallel plates. While in Kopfsill and Homsy (1988, the movement of bubbles was induced by gravity; in our configuration it is induced by the capillary pressure gradient caused by the channel tapering. More difficult than modelling the driving forces is the calculation of drag forces that balance the driving forces. The drag can be assumed to result from the same effects in a tapered channel as in a Hele-Shaw Cell.

As long as there is no inlet and outlet flow to the system, the space opened by a moving gas bubble must be balanced by liquid moving in the opposite direction. As the viscosity of the liquid is much higher than the viscosity of the gas, as considered by Tanveer (1987) and Taylor and Saffman (1959), the drag of a bubble in a Hele-Shaw Cell can be modelled in a first approximation by the viscosity of the embedding liquid, only. However, experiments performed and documented in Kopfsill and Homsy (1988) have shown a strong variation between experimental results and this simple model. Therefore, Tanveer (1987) and Taylor and Saffman (1959) extended their former work. In Saffman and Tanveer (1989), the drag forces induced by thin film deposition and dynamic contact angles were discussed to be the reason for the discrepancy between model and experiments.

Thin film deposition describes the effect of a liquid film deposited between channel walls and a moving gas bubble. It leads to a drag force at the beginning and the end of the bubble due to increased shear stresses there. Thin film deposition has been studied by Bretherton (1961) for the movement of gas bubbles in circular capillaries and was theoretically extended to polygonal capillaries by Wong et al. (1995a, b).

Contact angle dynamics has been already considered by Dussan (1979) and Hoffman (1975), but there is no conclusive theory about the phenomenon until today and several physical explanations are discussed in the literature, e.g. Hoffman (1975); Eggers and Stone (2004). In addition to increased shear stresses near the contact line and interface jumps on a molecular scale, the actual surface structure, in particular its roughness and chemical homogeneity play a decisive role (Schaffer and Wong 2000; de Gennes 1985). One empirical formula that describes the change of contact angle depending on the velocity of the contact line is given, e.g., by Bracke et al. (1989) based on a fit to experimental data.

Taking into to account these findings related to bubble dynamics in Hele-Shaw Cells, a model for the motion of a single gas bubble with constant volume in a tapered channel is presented in the first part of this article. In the second part, the model is calibrated against experiments and the results are discussed.

2 1D model for bubble movement in tapered channels

2.1 Bubble shape

In principle, a tapered channel can be considered to consist of two solid planes intersecting with an angle of 2α and the space between the planes filled with liquid. A gas bubble that is located in between the two planes deformed from its spherical equilibrium shape moves, whenever possible, straight towards the wider opening of the channel (Fig. 1) to minimize its surface energy. The movement happens only along one straight direction (the x-axis), while the bubble's shape and the shape change are intrinsically three-dimensional effects.

2.1.1 Capillary pressure

In every point of a bubbles surface, the capillary pressure jump from the inside to the outside of the bubble is given by the local mean curvature k and the interfacial tension between liquid and gas according to the Young–Laplace equation

$$p_{\mathrm{cap}} = \sigma k = \sigma\left(\frac{1}{r_1} + \frac{1}{r_2}\right) \tag{1}$$

The radiuses r_1 and r_2 belong to a couple of tangent radiuses to the interface in arbitrary but perpendicular directions (Finn 1986).

2.1.2 Equilibrium position

For a stationary gas bubble in equilibrium, the curvature is equal at any point of the interface. In case of a bubble in a wetting tapered channel (contact angle $\theta < 90°$), the equilibrium shape is basically a sphere. The sphere is cut off by the channel walls in a way that the contact angle has the correct value at every point of the contact line. The x-coordinate of the resulting sphere's centre x_{m} is equivalent to the centre of a spherical meniscus of the same radius in a wedge for which a formula is given in Langbein (2002).

2.1.3 General shape

A bubble that is squeezed in a tapered channel in a non-equilibrium position in general does not exhibit a surface of constant curvature. However, if the tapering angle approaches zero, the situation becomes equivalent to a Hele-Shaw Cell where a squeezed bubble attains the shape of a tin. As the tapering angles considered here are small, the shape of a squeezed bubble in the tapered channel can be approximated as a perturbation of such a tin body (Fig. 2). Due to the rotational symmetry, a bubble in a Hele-Shaw Cell must exhibit a circular projection when looking from top. In side view, the bubbles shape is substantially bounded by circular arcs intercepting the plates with the given contact angle.

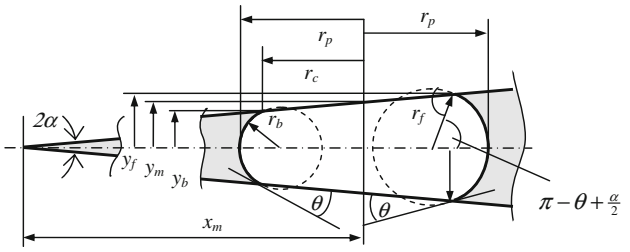

Fig. 3 Parameterization of a deformed bubble in a tapered channel

For a bubble in the tapered channel as sketched in Fig. 3, it is assumed that the projection of the bubble is still a circle (radius r_{p}), but perpendicular to this direction the bubble is modelled to be bound by varying circular arcs in any position i around the bubble with varying radii r_i. The radius r_i of any of these arcs is substantially a function of the local channel height and the contact angle θ. It can be calculated from these parameters.

In this approximation, the bubble shape is completely defined by the bubble volume, the distance of the bubble's centre towards the interception of the planes x_{m} and the contact angle θ. The relation between these parameters and the circular arcs necessary to calculate the capillary pressure is solved numerically in this article as explained below.

2.1.4 Bubble volume calculation

A bubble with volume V_{bub} and centre position x_{m} exhibits a deformation characterized by the resulting projection radius $r_{\mathrm{p}}(x_{\mathrm{m}}, V_{\mathrm{bub}}, \theta, \alpha)$ which is necessary to calculate the resulting capillary force. The calculation of the projection radius is done by the following predictor corrector scheme

$$\begin{aligned}
&1.)\ r_{\mathrm{p}}^{\mathrm{pre}} = r_{\mathrm{p}}(t - \Delta t)\\
&2.)\ V'_{\mathrm{bub}} = V_{\mathrm{bub}}\left(x_{\mathrm{m}}(t), r_{\mathrm{p}}^{\mathrm{pre}}, \alpha, \theta\right)\\
&3.)\ \Delta V_{\mathrm{bub}} = V'_{\mathrm{bub}} - V_{\mathrm{bub}}\\
&4.)\ r_{\mathrm{p}}^{\mathrm{corr}} = -\frac{1}{3} r_{\mathrm{p}}^{\mathrm{pre}} \frac{\Delta V_{\mathrm{bub}}}{V_{\mathrm{bub}}}\\
&5.)\ r_{\mathrm{p}}^{\mathrm{pre}} = r_{\mathrm{p}}^{\mathrm{pre}} + \lambda r_{\mathrm{p}}^{\mathrm{corr}}\\
&6.)\ \rightarrow 2.)
\end{aligned} \tag{2}$$

First, a guess for the projection radius $r_{\mathrm{p}}^{\mathrm{pre}}$ is made. During dynamic calculations, the value of r_{p} from the previous time step is used. For the initial calculation, a rough estimation for $r_{\mathrm{p}}^{\mathrm{pre}}$ is made by approximating the bubble as a flat cylinder with the same mean height y_{m} as the gas bubble. This height is the product of the position x_{m} and opening angle $\tan\alpha$. The bubble volume can be

parameterized straightforward and explicitly in the form $V_{bub} = V_{bub}(x_m, r_p, \alpha, \theta)$ using the assumptions made in Sect. 2.1.3. In step 2.), the bubble volume is calculated at the new position x_m using the predictor value r_p^{pre}. With the deviation in the resulting value for the bubble volume ΔV_{bub} calculated in step 3.), the error in the projection radius r_p^{corr} is estimated by an error propagation law 4.). In step 5.), the predictor value is corrected with the estimated error where an under relaxation factor λ $(0 < \lambda < 1)$ is used to preserve numerical stability. The scheme is repeated until the relative error in the volume calculation is smaller than a given criterion.

2.2 Equation of motion

The movement of a gas bubble is modelled as a one-dimensional equation of motion for its centre position x_m. The bubble is accelerated by the capillary force F_{cap} resulting from the different curvatures at both ends. This force is balanced by different drag forces D that decelerate the bubble to a finite velocity

$$\begin{aligned} \frac{dx_m}{dt} &= v(t) \\ \frac{dv}{dt} &= \frac{1}{m}\left[F_{cap}(x_m) - D(x_m, v(t))\right] \end{aligned} \tag{3}$$

The necessary mass in Eq. 3 is approximated to be proportional to the mass of a fraction of liquid having the same volume as the gas bubble

$$m = C_{inertia}\rho_{liq}V_{bub} \tag{4}$$

While the mass accelerated in reality is unknown and may even change during a bubbles movement, this mass is chosen in the model to provide at least similarity when scaling the problem. The calibration factor $C_{inertia}$ accounts for the difference of the approximated mass to the effectively moving mass. During calibration, it was found that the inertial term is small compared to the other forces and an error in estimating the mass is not affecting the solution significantly. Nevertheless, a finite mass is necessary in the model to limit the initial acceleration while a bubble starts moving.

To calculate the capillary force F_{cap} that drives the gas bubbles one would have to integrate the capillary pressure, defined by the local radii at any point of the gas bubbles surface over this surface. Due to the symmetry, only the resulting force vectors in direction of the movement (positive x-coordinate) are relevant. As the projection radius is assumed to be constant all around the gas bubble, only the vertical arcs are of interest. The force parts of all vertical arcs are inversely proportional to their radius and the $\sin\gamma$, where γ parameterizes the position around the bubble projection as shown in Fig. 2 (left). The radius can be assumed to increase linearly from r_b at the backside of the bubble towards r_f at the front. The capillary force increases proportional to $\sin\gamma$ from $\sigma/r_b dA$ towards $\sigma/r_f dA$. Without performing the integration completely, the driving capillary force F_{cap} is modelled only by the orthogonal radiuses r_f and r_b (Fig. 3) within the considered approximation

$$F_{cap} = C_{cap}A_{ref}\sigma\left(\frac{1}{r_b} - \frac{1}{r_f}\right) \tag{5}$$

A reference area A_{ref} accounts for the projection area on which the forces are approximately acting. It is chosen as half the surface of a cylinder embedding the bubble with radius r_p and height $x_m \tan\alpha$. This area is proportional to the height and the width of the bubble and thus meters the force the bubble exerts in the frontal direction.

$$A_{ref} = \pi r_p x_m \tan\alpha \tag{6}$$

2.3 Drag forces

The drag D (x_m, v) in Eq. 3 is modelled as a superposition of forces acting on the moving bubble. Four possible drag effects are taken into account

- viscous flow in the surrounding liquid D_{visc}
- deposition of thin films D_{film}
- contact angle hysteresis or pinning D_{pin}
- contact angle dynamics D_{dc}

$$D = D_{visc} + D_{film} + D_{pin} + D_{dc} \tag{7}$$

The four used drag terms will be discussed in detail in the following.

2.3.1 Viscous drag

While a bubble moves forward, the surrounding liquid is displaced into the opposite direction and experiences viscous dissipation. The resulting drag has been calculated for a Hele-Shaw Cell in Taylor and Saffman 1959. As the Reynolds number Re is low, the pressure gradient in the surrounding liquid is calculated with the bubbles mean velocity according to the lubrication equation with given channel height h

$$\frac{dp}{dx} = \frac{12\eta}{h^2}v \tag{8}$$

The viscous flow of liquid occurs in a virtual channel next to the bubble with dimensions proportional to the bubbles mean height and the bubbles mean length. This results in the viscous drag

$$D_{visc} = \int_A \int_{x-r_p}^{x+r_p} \frac{dp}{dx} dx dA = C_{visc}A_{ref}r_p\frac{8\eta}{y_m^2}v \tag{9}$$

2.3.2 Thin film deposition

As mentioned, a bubble moving along a wall deposits a thin film of liquid between the bubble and the wall. The film separates the gas phase partly or completely from the solid wall. It has been shown for different structures (Bretherton 1961; Wong et al. (1995a, b); Probstein 2003) that the thickness of the film as well as the drag of a bubble scales with the capillary number by a power of $Ca^{2/3}$. The induced force depends on the capillary pressure that pushes the liquid between bubble and wall. The drag induced due to thin film deposition is modelled by Eq. 10

$$D_{\text{film}} = C_{\text{film}} A_{\text{ref}} \frac{\cos\theta\sigma}{y_{\text{m}}} \text{Ca}^{2/3} \tag{10}$$

Again the constant C_{film} is a priori unknown and will be calibrated by experiments later.

2.3.3 Contact angle hysteresis

It is well known in literature (Dussan 1979; Eggers and Stone 2004; de Gennes 1985) that the contact angle of an advancing meniscus is mostly larger than the contact angle of a receding one. Without dependence on the actual velocity of movement, this induces a threshold force on the moving meniscus which has to be considered at both ends of a moving bubble. For a μDMFC, this was considered, e.g., by Wong et al. (2005). The threshold or pinning force must be overcome to initiate a bubble movement at all. The poinning force is hard to model by elementary laws (Schaffer and Wong 2000) as it depends strongly on the given surface conditions. To take the effect into account, a very simple model is set up here. It assumes only that the total pinning force is proportional to the length of the contact line of the gas bubble and the surface tension.

$$D_{\text{pin}} = C_{\text{pin}} \pi \sigma r_{\text{c}} \tag{11}$$

In Eq. 11, r_{c} denotes the radius of the contact line of the bubble that decreases, while the gas bubble moves towards the wider opening of the channel. Obviously, the proportionality C_{pin} in Eq. 11 must depend on the surface properties and cannot have universal character.

In general, contact angle hysteresis can be measured. During the experiments performed here, the static contact angle was determined experimentally to be around $\theta = 9°$ through all experimental configurations. Contact angle hysteresis is hard to measure for such small contact angles at all. As $\cos\theta$ is 0.98 at $\theta = 9°$, even a doubling towards $\theta = 18°$ with $\cos\theta = 0.95°$ would not affect the problem strongly. Therefore, the constant C_{pin} has also been determined by calibration through the experiments without measuring contact angle hysteresis. As will be seen later D_{pin} has no significant influence in the model, which further justifies this simplification.

2.3.4 Contact angle dynamics

During movement of a gas bubble, the contact angle changes as a function of the velocity of the contact line as well. This dynamic contact angle is implemented in terms of the empirical model derived in Bracke et al. (1989). The so called Bracke formula in Eq. 12 describes the dynamic contact angle θ_{d} as a function of the static value θ_{s} and the dimensionless capillary number Ca

$$\cos\theta_{\text{d}} = \cos\theta_{\text{s}} \pm 2(1 + \cos\theta_{\text{s}})\sqrt{\text{Ca}} \tag{12}$$

The model was used because of its character as a power law that can be compared straightforward to other power laws. By van Mourik et al. (2005), it is shown that the numerical evaluation of Eq. 12 delivers comparable values to a number of other models. An uncertainty of the model is that it is symmetric around the static contact angle. This is not fatal in the current work, as the receding contact angle is always close to zero. For other material combinations, more elaborated models may have to be used to account for this.

The change in contact angle induces a change in curvature between the front and the back of the bubble. This in turn induces a difference in the capillary pressure drop at the front and rear side of the bubble. The resulting drag force D_{dc} accounting for this difference is calculated here explicitly as

$$D_{\text{dc}} = C_{\text{dc}} 2\sigma A_{\text{ref}} (1 + \cos\theta)\sqrt{\text{Ca}} \left(\frac{1}{y_{\text{b}}} + \frac{1}{y_{\text{f}}} \right) \tag{13}$$

3 Experiments

3.1 Dimensional analysis

In order to be able to determine and to qualify the experimental parameter sets regarding their initial conditions, a dimensional analysis was performed according to the Π-Theorem (Buckingham 1914). Seven parameters where found to dominate the problem (Table 1).

Table 1 Parameters that define the starting condition for a moving bubble in a tapered channel

Parameter	Symbol	Unit
Half opening angle	α	° (none)
Contact angle	θ	° (none)
Bubble volume	V	m^3
Centre position or projection radius at start	$x_{\text{m0}}/r_{\text{p0}}$	m
Viscosity	η	kg m^{-1} s^{-1}
Surface tension	σ	s^{-2} kg
Density	ρ	kg m^{-3}

Table 2 Four dimensionless numbers are characteristic for a single experiment

Dimensionless Number	Symbol	Building law
Half opening angle	α	α
Contact angle	θ	θ
Squeezing parameter	Sq	$\mathrm{Sq} = \frac{r_{p0}}{\sqrt[3]{\frac{3}{4\pi}V}}$
Ohnesorge number	*Oh*	$Oh = \frac{\eta}{\sqrt{\sigma r_s \rho}}$

According to the Π-Theorem, four dimensionless numbers are sufficient to characterize the initial conditions of a single experiment as this is the difference between the number of parameters (seven) and basic units (three) in the system (Table 1). The set of dimensionless numbers chosen in this work is given in Table 2.

3.1.1 Half opening angle α

The half opening angle α is a fixed dimensionless number that characterizes the tapering of the channel and is considered to be small in order to stay within the limits of the geometrical approximations. It can be interpreted as the relative change of the bubble shape per channel length. In the performed experiments, α was varied systematically.

3.1.2 Squeezing parameter Sq

To characterize the initial shape of a bubble before it starts moving, the squeezing parameter Sq is introduced. It is defined as the ratio between initial projection radius r_{p0} and the radius of a sphere—the equilibrium shape in the tapered channel for small contact angles—with the same volume as the deformed bubble

$$\mathrm{Sq} = \frac{r_{p0}}{\sqrt[3]{\frac{3}{4\pi}V}} \tag{14}$$

The parameter Sq rates the initial deformation of the bubble, and therefore the potential energy that can be released during the movement. In the experiments, the squeezing parameter was varied by varying the starting position of bubbles of constant volume during the experiments.

3.1.3 Ohnesorge number Oh

All material parameters together with the absolute dimension of the problem are summarized within the Ohnesorge number. Therefore, it contains the dimensional scaling behaviour of the system and describes how the viscous damping grows over capillary and inertial forces with miniaturization of the system. The total dimension is represented by the radius of the equivalent sphere of the given bubble volume like in the definition of the squeezing parameter above. In the experiments, the Ohnesorge number was varied mainly by varying the content of isopropyl alcohol in the mixture with water as liquid phase

$$Oh = \frac{\eta}{\sqrt{\sigma \sqrt[3]{\frac{3}{4\pi}V}\rho}} \tag{15}$$

3.1.4 Contact angle θ

The (static) contact angle is a dimensionless number itself. In the presented experiments, it was kept constant and measured to be $\theta = 9° \pm 2°$.

3.2 Experimental setup

The basic experimental setup to study the bubble dynamics in a tapered channel is shown in Fig. 4. Two glass slides where clamped together with a well-defined tapering angle to form the channel walls. Liquid introduced between the glass slides is kept there by capillary forces. At the narrow edge of the assembly, a micro pipe (ø 80 µm) is used as a gas inlet. The air flow is controlled manually via a pinch valve and a throttle in the inlet channel. In the arrangement, the direction of the bubbles centre of movement is tilted by the angle α. The resulting buoyant force is small compared to the other forces for most of the travelling distance of the gas bubble, except the equilibrium position, where the other forces vanish (see Fig. 5).

Bubbles are formed in the liquid between the glass slides when the inlet pressure overcomes the capillary pressure of the micro pipe. Bubbles break off from the pipe at a certain size. The bubbles are observed by a camera from the top of the slides with a maximum frame rate of 90 frames per second. Self made image processing software using the OpenCV library from Intel (2001) was used to identify the bubbles and trace them over time. The bubble volume was calculated from the bubbles diameter at the equilibrium position by assuming a spherical shape there. As liquid

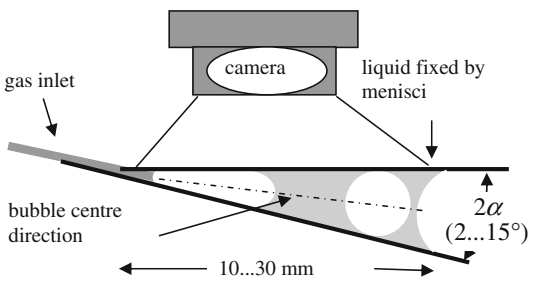

Fig. 4 Experimental setup: two glass slides arranged with a predefined opening angle. Air is introduced through a micro pipe from the left. Bubbles grow and break off from the inlet. The movement is recorded by a camera from the top

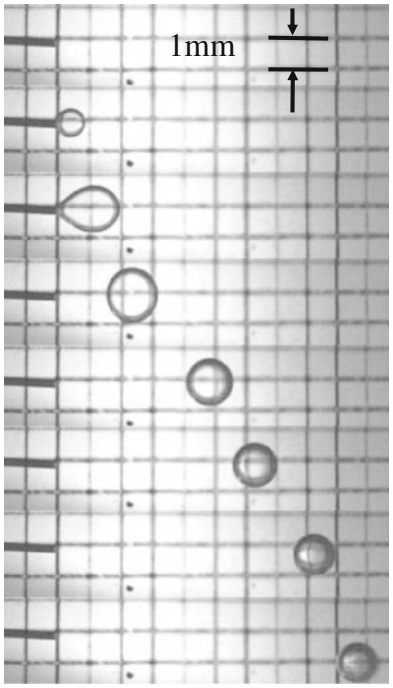

Fig. 5 Sequence of a gas bubble moving from left to right in a tapered section recorded by the experimental setup

Table 3 Material parameters of the isopropyl alcohol in water mixtures used in the experiment

Part propyl alcohol (g/l)	ρ (kg m^{-3})	η (mPa s)	σ (m Nm^{-1})	θ (°) (glass)
0	1,000	1.0	72.5	9 ± 2
60	983	1.30	44.0	9 ± 2
120	967	1.71	35.12	9 ± 2

The contact angles were measured on glass slides. The uncertainty is about ±2°

phase three mixtures of isopropyl alcohol in water were used (Table 3). Viscosity, contact angle on the glass slides and the density were measured. Values for the surface tension were used from a reference measurement from imeter (2006).

In preparation to the main experimental series, the process of droplet break was investigated. While the break up frequency varies with the inlet pressure, the bubble size is constant and depends on the opening angle and the inlet position, only. It was found that with variation of the inlet position, the squeezing parameter Sq varies stronger than the Ohnesorge number.

3.3 Performed experiments

Experiments were performed for twelve parameter sets. The registered bubble trajectories were averaged over 10 to 30 bubbles for every parameter set. The initial conditions of the experimental sets are documented in Table 4.

The opening angle was varied at small values in a range relevant for the application of capillary driven bubble flow in microfluidic applications. Variation of the inlet position led to a slight variation of the squeezing parameter Sq. A stronger variation of the squeezing parameter Sq was observed in connection with the opening angles—nearly independent of the Ohnesorge number. In contrast the variation of the Ohnesorge number with different mixtures of water to propyl alcohol is up to a factor of four.

3.3.1 Ink experiments

To qualitatively investigate the characteristics of the flow around the moving gas bubbles, experiments with ink were

Table 4 Characteristic numbers of experiments

Experimental setup	Dimensionless parameters			Physical parameters		
	Tapering angle 2α (°)	Squeezing parameter Sq	Ohnesorge number (1/100)	Contat angle θ (°)	Part propyl alcohol (g/l)	Bubble volume (µl)
1)	5.5	1.66	1.31	9	120	0.53
2)	5.5	1.61	1.21	9	120	8.63
3)	5.5	1.58	1.16	9	120	1.09
4)	5.5	1.60	1.11	9	120	1.40
5)	5.5	1.43	1.05	9	120	2.04
6)	5.5	1.36	1.02	9	120	2.32
7)	3	1.89	1.11	9	120	1.44
8)	4	1.77	1.13	9	120	1.28
9)	7	1.58	1.08	9	120	1.72
10)	10	1.37	1.07	9	120	1.76
11)	5.5	1.80	0.39	9	0	3.09
12)	5.5	1.63	0.82	9	60	8.39

Bubble volume and radius calculated from measured equilibrium position

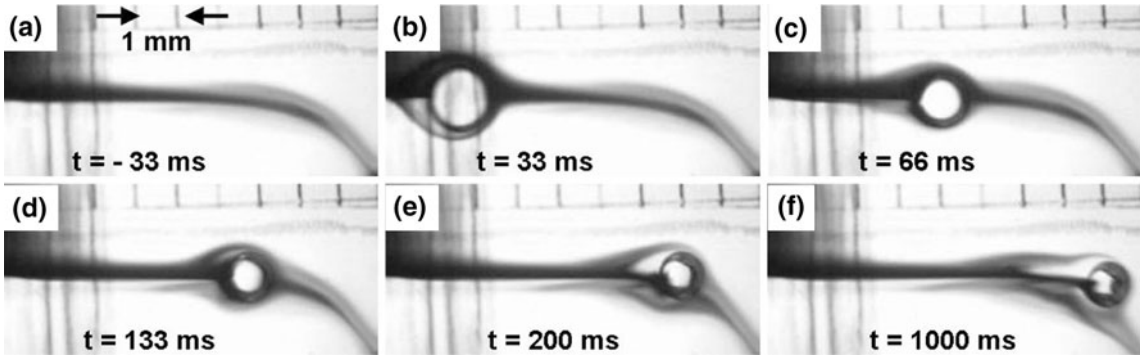

Fig. 6 Flow around a moving gas bubble in a tapered channel section visualized by ink

performed as shown in Fig. 8. A droplet of diluted ink (density and viscosity similar to water) was induced at the starting point of the gas bubbles near to the inlet pipe. The ink is transported with the gas bubbles along their path of movement. After some gas bubbles were moving a thread of ink marks the bubble path. This thread can be used to visualize some characteristics in the flow around the following gas bubble qualitatively as shown in Fig. 6. The gas bubble travels from left to right. The setup was slightly tilted perpendicular to the direction of movement so the gas bubbles path turns near the equilibrium position and the bubbles are removed from the area of interest by buoyancy. For this reason, the ink track is not straight, but makes at turn at its end.

From Fig. 6 several aspects of the experiment can be observed. First, until near the end position, no swirling of the flow occures which confirms laminar flow conditions. Only near the end position some kind of detached flow around the bubble can be suspected (Fig. 6e, $t = 200$ ms). Therefore, in the main path the flow field around the bubble has substantially the characteristics of a laminar flow around a cylinder, and the disturbance of the flow by the moving gas bubble decreases at least with r^{-1}. Therefore, the interaction of the gas bubbles with the side boundaries can be neglected as the boundaries are at least 10 bubble diameters away ("wide" channel approximation) and the main simplifications of the presented model are confirmed.

4 Model calibration

4.1 Full model

In the experiments, the x-coordinates of the centre of the moving gas bubbles are recorded as a function of time $x_m(t)$ to calibrate and validate the proposed model. Therefore, a genetic algorithm called differential evolution by Storn and Price (1997) is used. The equation system Eq. 3 is solved numerically with a trial set of coefficients (C_{inert}, C_{visc}, C_{film}, C_{pin}, C_{dca}). One coefficient in Eq. 3 can be arbitrarily selected. As the capillary pressure difference is the best known effect and therefore its value can be estimated most accurately, C_{cap} is set to one.

The simulated bubble trajectories are compared to those trajectories derived from the experiments. The error δ between the model results $\tilde{x}_i(t)$ and the experimental graphs $x_i(t)$ is minimized through genetic evolution of the coefficients. For every experimental set, the error δ_i is calculated according to Eq. 16

$$\delta_i = \frac{1}{\left(x_{i,\max} - x_{i,\min}\right)^2} \int |x_i(t) - \tilde{x}_i(t)| \frac{\mathrm{d}}{\mathrm{d}t} x_i(t) \mathrm{d}t \tag{16}$$

Equation 16 is a parameterized integration of the deviation between the simulation results and the experimental data with the time t as parameter. The error calculation is performed numerically with high resolution (400 points per trajectory). As the calculation of errors incorporates both, bubble position and velocity, errors in the final static position that result from errors in measuring the bubble volume are not weighted. The cumulative error δ that is minimized during the genetic evolution is built from the mean value $\bar{\delta}_i$ of the errors for every experimental set and their standard deviation according to Eq. 17

$$\delta = \bar{\delta}_i + \sqrt{\frac{1}{N} \sum \left(\delta_i - \bar{\delta}_i\right)^2} \tag{17}$$

This ensures that the calibration has comparable quality for all experimental sets.

As an example, the experimentally recorded and the simulated bubble trajectories are plotted in Fig. 7 for the second experimental set as given in Table 4. Results for all experimental sets are given in the appendix.

The cumulative error for the calibration of all 12 experiments was 5.2%. The resulting parameters are given in Table 5.

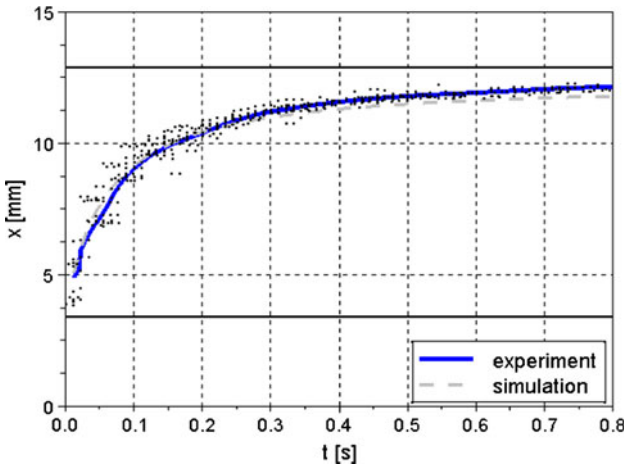

Fig. 7 Bubble position over time. *Light dashed* simulation curve; *thick black* average of experimental data; *dots* raw data of measurements for several bubbles. (Parameter set Nr. 2)

Table 5 Coefficients for the model derived from calibration

Coefficient	Fitted value
C_{inert}	2.62 E-2
C_{cap}	1
C_{visc}	1.00
C_{film}	2.11
C_{pin}	1.45 E-4
C_{dc}	0.044

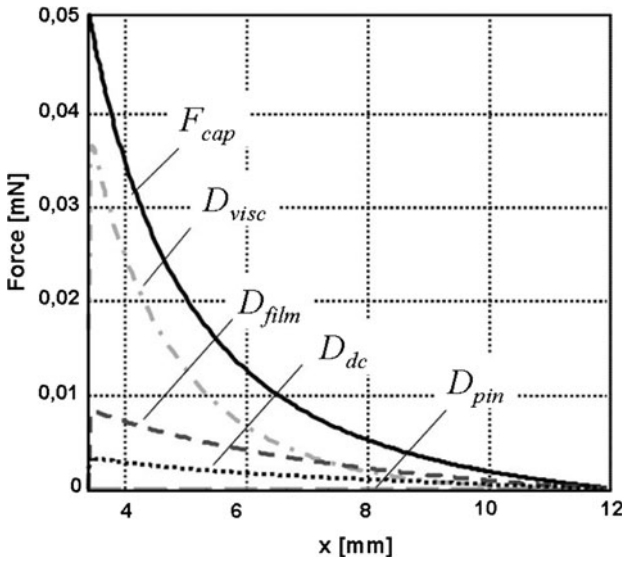

Fig. 8 Forces on the bubble as derived from the simulation over position (Parameter set Nr. 2)

It is not possible to directly compare the effects of different drag forces on a bubbles movement from the dimensionless coefficients given in Table 5. To perform a comparison, the absolute forces on the bubble as deduced from the simulation have to be studied. The forces are plotted in Fig. 8 for one parameter set (Nr. 2).

The graphs for the other parameter sets look similar. From Fig. 7, it is obvious that the viscous drag D_{visc} dominates the problem at the beginning of the movement where the velocities are high and the channel is narrowest. At moderate velocities in the middle section between seven and eight millimetres the dynamic contact angle D_{dc} and thin film drag D_{film} overcomes the viscous drag and a superposition of all the effects governs the dynamics. While the second half of the graph in Fig. 8 shows only small forces it covers half the way the bubble moves. When looking at the same position of about 7.5 mm in Fig. 7, one finds that this position is reached already at about 50 ms, while still at about 1 s the bubble has not reached its equilibrium position. Thus more than 90% of the time, the viscous term does not dominate the movement. Even for the small opening angle $2\alpha = 5.5°$ most of the energy stored in a deformed bubble is released at a very short distance of the gas bubbles path. This can be seen from the steep decrease in the capillary pressure force F_{tot}. While the bubble is initially strongly deformed, it relaxes very fast from a merely flat towards a merely spherical shape and with decreasing deformation and therefore energy release, it moves finally very slow towards the equilibrium position.

The pinning term D_{pin} can be found to be negligible in the presented experiments. On the one hand, this results from the small advancing static contact angle of only $\theta = 9°$ and the good surface quality of the glass slides, and on the other hand from the fact, that the contact line seems to vanish during movement at all. Probably, the assumption that the bubble becomes completely detached from the walls would be justified in this case, as well. The presented model could account for this assumption by setting $D_{\text{pin}} = 0$ (see Sect. 4.1.1).

As the path of the gas bubbles centre is not horizontal in the experiments buoyancy must be discussed. Buoyancy can be incorporated in the model as a force given by

$$F_{\text{buo}} = p_{\text{buo}} A_{\text{ref}} = 2\left(\rho_{\text{liq}} - \rho_{\text{air}}\right) g \tan\alpha \; y_{\text{m}} \; A_{\text{ref}} \tag{18}$$

In Eq. 17, only the horizontal fraction of the buoyant force is relevant. It is proportional to $\sin\alpha$. The maximum value of F_{buo} was found to be about two orders of magnitude smaller than the initial driving capillary force induced by the squeezing of the gas bubbles. In Table 6, values for the initial parameters are given for all experimental sets together with results for the capillary pressures taken from the simulations performed with the calibrated model. Also values for the buoyant pressure p_{buo} in the equilibrium position using Eq. 17 are given in Table 6. As the bubble height reaches its maximum buoyancy has its maximum there, too. Keeping further in mind that during the model

Table 6 Characteristic dimensions of the experimental sets and calculated values using the calibrated model

Experimental setup	Tapering angle 2α (°)	Projection radius at start r_p (mm)	Mid bubble position x_m at start (mm)	Mid bubble height $2y_m$ at start (mm)	Maximum capillary pressure (Pa)	Reference area in start point A_{ref} (mm^2)	Buoyant pressure at equilibrium position (Pa)	Equilibrium position (mm)	Equilibrium radius (mm)
1)	5.5	0.83	2.73	0.26	150	0.69	0.50	11.0	0.50
2)	5.5	0.95	3.42	0.33	105	0.98	0.59	12.9	0.59
3)	5.5	1.01	3.86	0.37	85.4	1.18	0.62	13.6	0.64
4)	5.5	1.11	4.07	0.39	86.2	1.36	0.65	14.1	0.69
5)	5.5	1.12	5.99	0.57	34.9	2.03	0.73	15.9	0.79
6)	5.5	1.12	7.04	0.68	23.2	2.37	0.75	16.3	0.82
7)	3	1.33	5.22	0.27	123	1.14	0.32	23.7	0.70
8)	4	1.20	4.33	0.30	119	1.14	0.50	20.6	0.67
9)	7	1.18	3.51	0.43	100	1.59	0.56	12.6	0.74
10)	10	1.03	3.43	0.60	53.9	1.94	0.93	9.2	0.75
11)	5.5	1.62	4.10	0.39	299	2.01	1.38	19.5	0.90
12)	5.5	0.96	3.28	0.31	146	0.95	0.89	12.9	0.59

Table 7 Shown are the results of the model calibration for different subsets ($C_{pin} = 0$)

Run	Model variation	Error (%)	C_{inert}	C_{visc}	C_{film}	C_{dc}
1	Full model	5.2	0.026	1.00	2.12	0.044
2	No dynamic contact angle ($C_{dc} = 0$)	5.0	0.0157	1.02	3.09	0
3	No thin film ($C_{film} = 0$)	5.6	0.0936	1.36	0	0.105
4	No thin film, no dynamic contact angle ($C_{film} = C_{dc} = 0$)	8.6	0.135	2.52	0	0

calibration the values near to the equilibrium position are weighted less, the effect of buoyancy on the quality of the calibration can be considered to be not significant. This has been verified by the authors by calculations including Eq. 17 in the calibrated model.

4.2 Variations

As the model is calibrated for a rather large number of free parameters, some variations were performed to validate the calibration. In order to test whether the full model is necessary to describe the problem or if a subset of drag terms are already a sufficient description, three subsets of coefficients where fitted against the experimental data. In those calculations, the pinning term was neglected at all. Resulting cumulative errors for the best fitting coefficient sets are given in Table 7.

From Table 7, one can find that the model can be calibrated with nearly the same quality while either the dynamic contact angle drag or the thin film drag is neglected. Without both sub models the error raises by about 40% from 5.2 to 8.6%.

Considering Table 7, one finds that for the different calibrations, the values for different coefficients vary. From the variations, the change of the relative influence of a drag model from one coefficient set to another can be estimated. Obviously, the relation between viscous and capillary coefficient varies only slightly in the first three runs. Also, the thin film coefficient C_{film} and the dynamic contact angle coefficient C_{dc} increase by about 50–100% if one of both is neglected. From this, it can be stated that those two effects are able to replace each other to a certain extent. This is not surprising as both drag terms scale with the radius of the contact line and the capillary number with similar power laws. The power law for the dynamic contact angle as used here (Bracke et al. 1989) is 1/2, while the power law for thin film deposition is 2/3. From a physical point of view this also makes sense as in the literature (Dussan 1979; Marsh et al. 1993) dynamic contact angles are sometimes explained as a result of increased shear stress near a moving contact line. On the

other hand, increased shear stresses are the explanation for forces coming along with thin film deposition (Bretherton 1961; Wong et al. 1995a, b) near the contact line as well. A closer look to the front end of a moving bubble (Fig. 5) reveals that it is difficult to distinguish whether a thin film is deposited or to what extent the contact angle is varied. Both effects may interleave depending on the material and local velocity and once a complete thin film covers the space between gas bubble and wall contact angle dynamics can not have an effect anymore. A dynamic contact angle may be the starting point for forming a thin film.

From a practical point of view, it is advantageous that both effects have quantitatively the same effect onto the movement of the gas bubbles in the derived model. This enables the use of the model even if the transition between dynamic contact angle and thin film deposition cannot be clarified. A conclusive understanding of those effects on the bubble movement in tapered structures may result only from higher resolution CFD-simulations with sophisticated models for the contact line dynamics.

5 Discussion

The derived overall accuracy of the model justifies its use to study the movement of gas bubbles in tapered channel sections. From the variation discussed in the previous section the model can be used in a simplified form containing only two drag terms. In this parameter range even the effect of growing gas bubbles can be applied, as it is simple to add a source term into the volume calculation.

5.1 Validity

The parameter space in which the current calibration of the model is valid can be derived from Table 4. While the contact angle was kept constant, the spanning of the parameter space in the three dimensions tapering angle, squeezing parameter and Ohnesorge number is of special interest. The bubble break up was not controlled externally, and therefore the parameters could not be varied completely independently.

As central parameter set the experiments 5) and 6) can be identified with tapering angles of 5.5° and a squeezing parameter about 1.4 as well as an Ohnesorge number about 1.05. The other parameter sets are distributed around this parameter set. A wide range could be achieved for the combination of contact angle and Ohnesorge number as both parameters were varied nearly independently for values from $Oh = 0.39 \times 10^{-2}$ to 1.31×10^{-2} and $2\alpha = 3°$–$10°$. The Ohnesorge number is affected by the material properties and by the absolute dimension of the bubble only, which could be kept nearly constant during variation of the opening angle. The squeezing parameter Sq had more correlation to the other parameters. With increasing Sq the Ohnesorge number also increased slightly and with decreasing opening angles, Sq changed.

Regarding Oh and Sq the parameter space from $Oh = 0.82 \times 10^{-2}$ to 1.31×10^{-2} and from Sq = 1.36 to 1.67 is well covered. Regarding 2α and Sq the parameter space from $2\alpha = 4°$ to 7° and from Sq = 1.36 to 1.89 is properly covered. Thus, a well-covered parameter space from $2\alpha = 4°$ to 7°, $Oh = 0.82 \times 10^{-2}$ to 1.31×10^{-2} and Sq = 1.36–1.89 can be identified. The additional parameter sets extend this parameter space only little.

5.2 Relevance for μDMFC

The range of opening angles from $2\alpha = 4°$ to 7° is interesting from a point of application as it offers a good compromise between strong capillary forces on bubbles and a useful distance for bubbles to travel. If the opening angle increases the travel range for a bubble from a minimal initial position towards its equilibrium position decreases compared to the radius of the bubble. Opening angles up to 7° are sufficient and useful. In Litterst et al. 2006, for example, opening angles of $2\alpha = 5°$ where successfully applied to μDMFCs.

The squeezing parameter correlates with opening angles in so far that for a given opening angle only a finite maximum squeezing parameter Sq_{max} is possible that is given once the backside meniscus of the squeezed bubble touches the interception of the two planes forming the tapered channel—a point of "infinite" capillary pressure. For Sq = 1, a gas bubble is at its equilibrium. To estimate Sq_{max} a simply approximation between volume and radius of a squeezed gas bubble can be performed by approximating the bubble as a cylinder of height $2\ y_m$ with y_m the half mean height of the gas bubble. This approximation neglects all bent parts and becomes exact only for the limit of maximum squeezed gas bubbles for very small opening angles. The radius of such a bubble can be compared to a bubble of same volume and spherical shape to receive an estimation of Sq_{max} depending on the opening angle Eq. 19

$$Sq_{max} = \sqrt[3]{\frac{2}{3}\frac{1}{\tan\alpha}} \tag{19}$$

For opening angles of $2\alpha = 3°$, Sq_{max} is 2.9 and for $2\alpha = 7°$ Sq_{max} is 2.2. These values are not possible to

reach even if Eq. 19 is exact because of the divergence of the capillary pressure at the narrow end of the channel. The upper limit of 1.89 achieved in the experiments relates to moderately squeezed bubbles having about half (compared to 2.2) or one-third (compared to 2.9) the radius deviation from the equilibrium value of 1. In practice, growing gas bubbles in micro reactors such like DMFC in particular if pinning is not present start moving much earlier, as soon as Sq is little larger than one.

The well covered range of *Oh* numbers is limited to values from 0.82 10^{-2} to 1.31 10^{-2} and is extended for a single case towards 0.39. Interesting are in particular values for methanol solutions in water as used in DMFC. The typical used 4 and 2 M solutions have the same mass of methanol diluted in water as propyl alcohol in the solutions used in this work. The contribution to surface tension and density of the mixtures are quite similar since propyl alcohol and methanol have similar values there (both $\sigma \sim 23$ m Nm^{-1}; $\rho_{\mathrm{prop}} = 790$ kg m^{-3} vs. $\rho_{\mathrm{meoh}} = 780$ kg m^{-3}). The main difference is that methanol has a much lower viscosity (0.55 m Pas vs. 2.05 m Pas). Thus the viscosity of methanol solutions in water can vary between 0.55 mPa s and 1 mPa s, and therefore the model is fitted for gas bubbles with diameters between 200 to 800 μm in this solutions. These are smaller than the gas bubbles used during the experiments. But these dimensions are in particular interesting for micro structured anode flow fields in DMFC. Thus, the model can be used for the design of such channel systems preferably.

5.3 Behaviour of gas bubbles in tapered channels

From the force plot in Fig. 7 and the bubble trajectories it can be found that the gas bubbles reach their highest velocities while being most squeezed. During this phase, the bubble drag is dominated by viscosity in the surrounding liquid. It is interesting to notice that the viscosity becomes less dominant for smaller velocities near to the equilibrium position of a gas bubble. There, in particular because of the larger channel diameter, other drag forces like contact angle dynamics become more relevant. From the ink experiments shown in Fig. 6, it is also found that at such positions the movement of gas bubble might induce also vortexes which may act back on the movement of the bubbles in this regime. For the application of gas bubbles in methanol fuel cells, this is interesting as for the mixing of methanol into the aqueous solution this behaviour can be advantageous. For the purpose of pumping or gas bubble removal the viscous regime may be more advantageous.

6 Conclusion

A 1D model for the movement of gas bubbles in tapered channels was proposed. The model was fitted against a range of experiments chosen on the basis of a dimensional analysis. The deviation between model and experiments is only about 5%. The model is valid in a range that is interesting for gas bubbles in micro structured flow fields for anodes of DMFC, exhibiting bubble diameters between 200 and 800 μm, a reasonable initial bubble deformation and channels with moderate tapering angles of up to 7°. Thus, the model can be a useful tool to predict the movement of gas bubbles in this range. In particular, it can be used as a fast 1D design tool for studying the movement of gas bubbles in dependence of tapering angle, fluid properties and start positions, e.g. for passive degassing structures of DMFC.

The model suggests that the effects of dynamic contact angle and thin film deposition have comparably influences onto the movement of the gas bubbles. This is reasonable from a physical point as both effects are partially explained in literature by increased shear stress near the contact line leading to similar power laws. Both effects together have about the same impact onto the movement of gas bubbles as the viscous dissipation in the embedding liquid. While the viscous dissipation seems to dominate for strongly squeezed bubbles at higher velocities and small channel heights, the contact line effects dominate the problem in particular at smaller velocities.

The performed experiments and their interpretation by the presented model underline the importance for future research in this field to gain a better understanding of the effects of dynamic contact angles and thin film deposition in this flow regime. While the model derived in this work enables calculation of the motion of gas bubbles in tapered sections for a parameter range of special interest, more complete field models that incorporate the underlying physical effects on the molecular scale are necessary to be used for many emerging applications of gas bubbles in micro channels of arbitrary geometry.

Acknowledgements This work was performed under support from the German Science Foundation (DFG) Grant ZE527/3, which is gratefully acknowledged by the authors.

Appendix

Experimental data

In this Appendix, the experimental data for all 12 performed experimental sets are given. The graphs contain the raw data as well as the result of the model derived in this

work. For every data set a polynom of order seven is given that was fitted to the mean values of the data. The coefficients are provided with the data, to reproduce the data by those coefficients, one has to put them into a polynomial series of the following form.

$$x(t) = \sum_{i=0}^{7} a_i t^i \tag{20}$$

See Fig. 9.

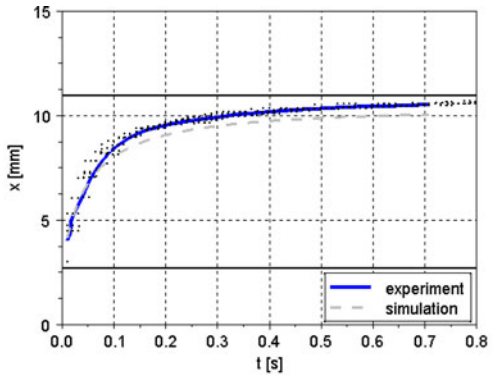

Setup 1: $2\alpha = 5{,}5°$; Sq = 1,66;Oh = 1,31E-2; $\theta = 9°$
(a_i: 4,12 E-3; 8,34 E-2; -5,40 E-1; 1,90; -3,63; 3,55; -1,39)

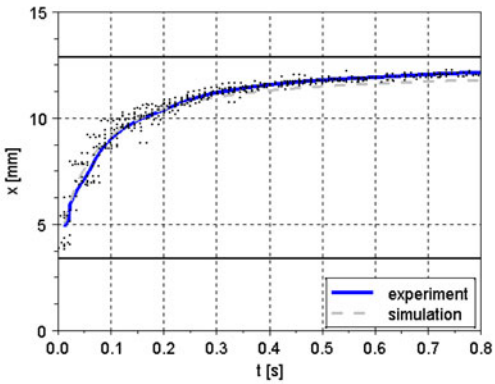

Setup 2: $2\alpha = 5{,}5°$; Sq = 1,61;Oh = 1,21E-2; $\theta = 9$
(a_i: 5,12E-3; 6,32E-2; -2,92E-1; 7,56E-1; -1,08; 7,88E-1; -2,3E-1)

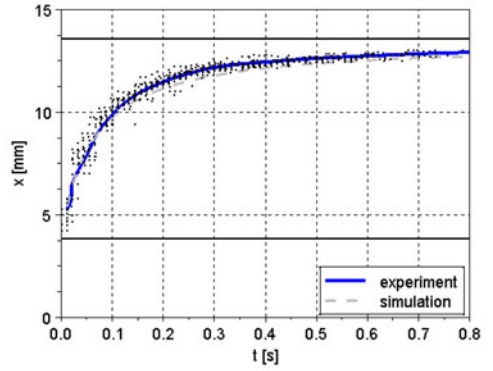

Setup 3: $2\alpha = 5{,}5°$; Sq = 1,58;Oh = 1,16 E-2; $\theta = 9°$
(a_i: 5,52E-3; 7,58E-2; -3,89E-1; 1,11; -1,77; 1,46; -4,8E-1)

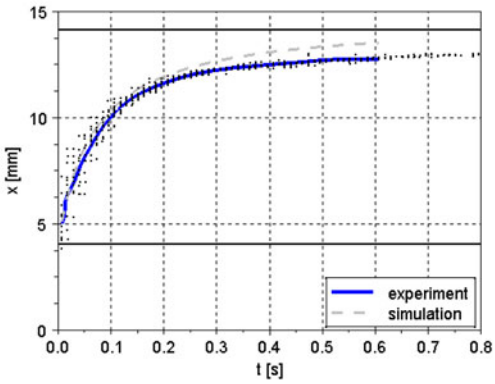

Setup 4: $2\alpha = 5{,}5°$; Sq = 1,60;Oh = 1,11E-2; $\theta = 9°$
(a_i: 5,24E-3; 8,62E-2; -5,13E-1; 1,83; -3,85; 4,38; -2,06)

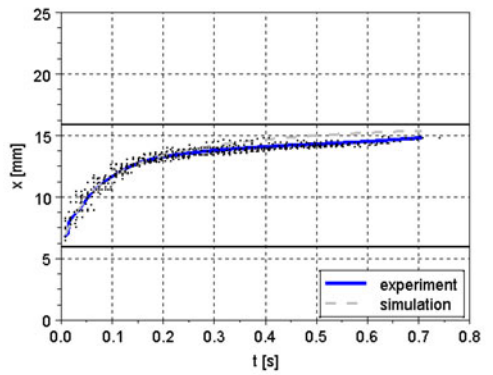

Setup 5: $2\alpha = 5{,}5°$; Sq = 1,43; Oh = 1,05 E-2; $\theta = 9$
(a_i: 8,33E-2; -4,66E-1; 1,47; -2,61; 2,44; -9,26E-1)

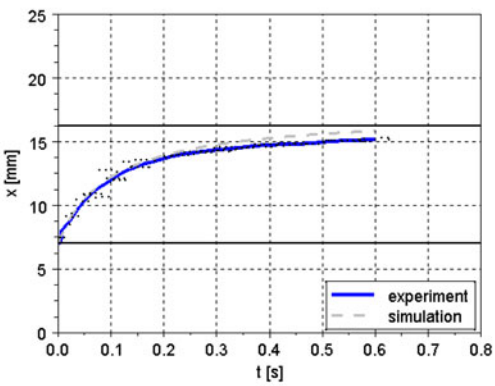

Setup 6: $2\alpha = 5{,}5°$; Sq = 1,36;Oh = 1,02 E-2; $\theta = 9°$
(a_i: 7,18E-3; 8,33E-2; -4,91E-1; 1,81; -3,96; 4,64; -2,22)

Fig. 9

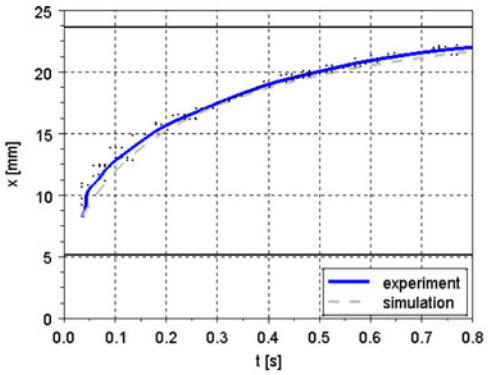

Setup 7: $2\alpha = 3°$; $Sq = 1{,}89$;$Oh = 1{,}11$ E-2; $\theta = 9°$
(a_i: 9,06E-3; 7,72E-2; -3,84E-1; 1,3; -2,44; 2,3; -8,57E-1)

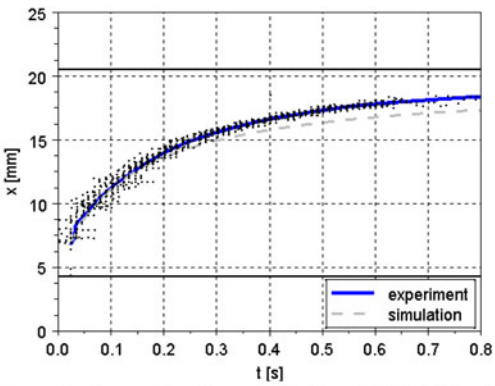

Setup 8: $2\alpha = 4°$; $Sq = 1{,}77$;$Oh = 1{,}13$ E-2; $\theta = 9°$
(a_i: 7,41E-3; 6,68E-2; -2,65E-1; 7,37E-1; -1,24; 1,11; -3,96E-1)

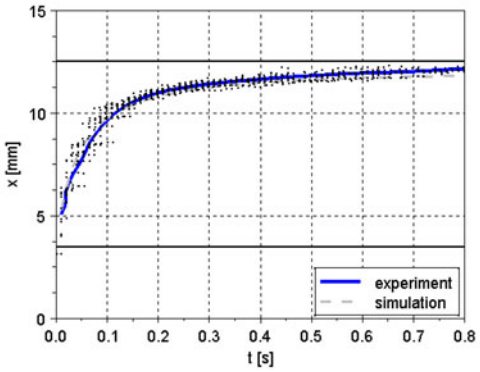

Setup 9: $2\alpha = 7°$; $Sq = 1{,}58$;$Oh = 1{,}08$ E-2; $\theta = 9°$
(a_i: 5,29E-3; 7,73E-2; -4,2E-1; 1,21; -1,89; 1,5; -4,72E-1)

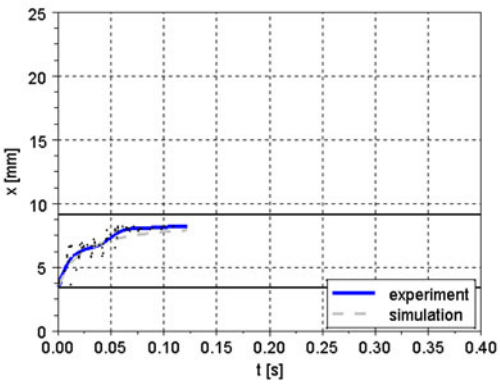

Setup 10: $2\alpha = 10°$; $Sq = 1{,}37$;$Oh = 1{,}07$ E-2; $\theta = 9°$
(a_i: 4,4E-3; 9,71E-2; -8,28E-1; 2,3; 5,43E-1; 9,12E-2; 1,34E-2)

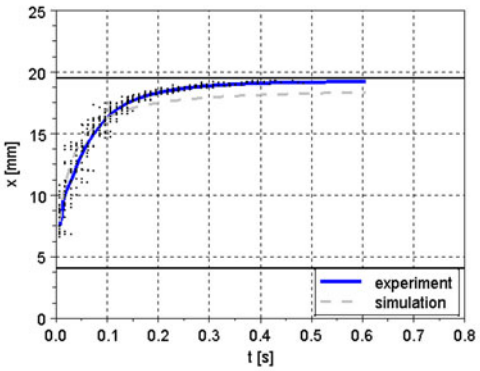

Setup 11: $2\alpha = 5{,}5°$; $Sq = 1{,}80$;$Oh = 0{,}39$ E-2; $\theta = 9°$
(a_i: 8,04E-3; 1,61E-1; -1,09; 4,11; -8,7; 9,65; -4,34)

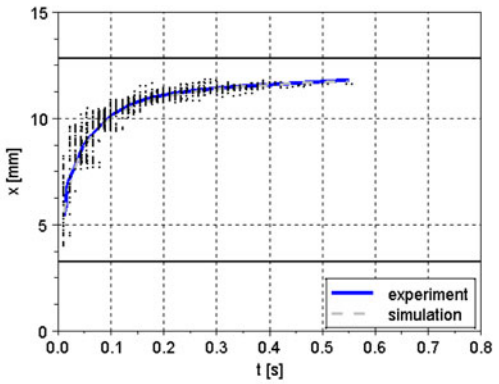

Setup 12: $2\alpha = 5{,}5°$; $Sq = 1{,}63$;$Oh = 0{,}82$ E-2; $\theta = 9°$
(a_i: 5,94E-3; 9,69E-2; -8,4E-1; 4,05; -1,07E+1; 1,45E+1; -7,85)

Fig. 9 continued

References

Bracke M, de Voeght F, Joos P (1989) The kinetics of wetting: the dynamic contact angle. Progr Colloid Polym Sci 79:142–149

Bretherton FP (1961) The motion of long bubbles in tubes. J Fluid Mech 10:166–188

Buckingham E (1914) On physically similar systems; illustrations of the use of dimensional equations. Phys Rev 4:345–376

de Gennes PG (1985) Wetting: statics and dynamics. Rev Mod Phys 57:827–863

Dussan EB (1979) Spreading of liquids on solid-surfaces—static and dynamic contact lines. Annu Rev Fluid Mech 11:371–400

Eggers J, Stone HA (2004) Characteristic lengths at moving contact lines for a perfectly wetting fluid: the influence of speed on the dynamic contact angle. J Fluid Mech 505:309–321

ESI-CFD (2006) CFD ACE+ 2006 simulation package

Finn R (1986) Equilibrium capillary surfaces. Springer, Stanford
Hoffman RL (1975) Study of advancing interface .1. Interface shape in liquid-gas systems. J Colloid Interface Sci, 50: 228-241
imeter/MSB Breitwieser Messsysteme (2006) Oberflächenspannung: Wasser/Isopropanol Konzentrationsabhängigkeit
Intel Corp. USA (2001) OpenCV—Open Source Computer Vision Library
Kopfsill AR, Homsy GM (1988) Bubble motion in a Hele-Shaw Cell. Phys Fluids 31:18–26
Litterst C, Eccarius S, Hebling C, Zengerle R, Koltay P (2006) Increasing μDMFC efficiency by passive CO_2 bubble removal and discontinuous operation. J Micromech Microeng 16:248–253
Marsh JA, Garoff S, Dussan EB (1993) Dynamic contact angles and hydrodynamics near a moving contact line. Phys Rev Lett 70(18):2778–2781
Paust N, Litterst C, Metz T, Eck M, Ziegler C, Zengerle R, Koltay P (2009a) Capillary-driven pumping for passive degassing and fuel supply in direct methanol fuel cells. Microfluid Nanofluid 7:531–543
Paust N, Krumbholz S, Munt S, Müller C, Koltay P, Zengerle R, Ziegler C (2009b) Self-regulating passive fuel supply for small direct methanol fuel cells operating in all orientations. J Power Sources 192:442–450
Probstein RF (2003) Physicochemical hydrodynamics: an introduction, 2nd edn. Wiley Interscience, Hoboke
Saffman PG, Tanveer S (1989) Prediction of bubble velocity in a Hele-Shaw Cell—thin-film and contact-angle effects. Phys Fluids A 1:219–223
Schaffer E, Wong PZ (2000) Contact line dynamics near the pinning threshold: a capillary rise and fall experiment. Phys Rev E61: 5257–5277
Storn R, Price K (1997) Differential evolution—a simple and efficient heuristic for global optimization over continuous spaces. J Global Optimi 11:341–359
Tanveer S (1986) The effect of surface-tension on the shape of a Hele-Shaw Cell bubble. Phys Fluids 29:3537–3548
Tanveer S (1987) New solutions for steady bubbles in a Hele-Shaw Cell. Phys Fluids 30:651–658
Taylor G, Saffman PG (1959) A note on the motion of bubbles in a hele-shaw cell and porous medium. Q J Mech Appl Math 12:265–279
van Mourik S, Veldman AEP, Dreyer ME (2005) Simulation of capillary flow with a dynamic contact angle. Microgravity Sci Technol 17:87–94
Wong H, Radke CJ, Morris S (1995a) The motion of long bubbles in polygonal capillaries.1. Thin-films. J Fluid Mech 292:71–94
Wong H, Radke CJ, Morris S (1995b) The motion of long bubbles in polygonal capillaries.2. Drag, fluid pressure and fluid-flow. J Fluid Mech 292:95–110
Wong CW, Zhao TS, Ye Q, Liu JG (2005) Transient capillary blocking in the flow field of a micro DMFC and its effect on cell performance. J Electrochem Soc 152:A600–A1605
Langbein D (2002) Capillary surfaces. Springer, Berlin
Yang H, Zhao TS, Ye Q (2004a) In situ visualization study of CO_2 gas bubble behavior in DMFC anode flow fields. J Power Sources 139:79–90
Yang H, Zhao TS, Ye Q (2004b) Addition of non-reacting gases to the anode flow field of DMFCs leading to improved performance. Electrochem Commun 6:1098–1103